Experimental approaches for micromagnetic coercivity analysis of advanced permanent magnet materials

Satoshi Okamoto

Taylor & Francis
Taylor & Francis Group

FOCUS ISSUE REVIEW

OPEN ACCESS | Check for updates

Experimental approaches for micromagnetic coercivity analysis of advanced permanent magnet materials
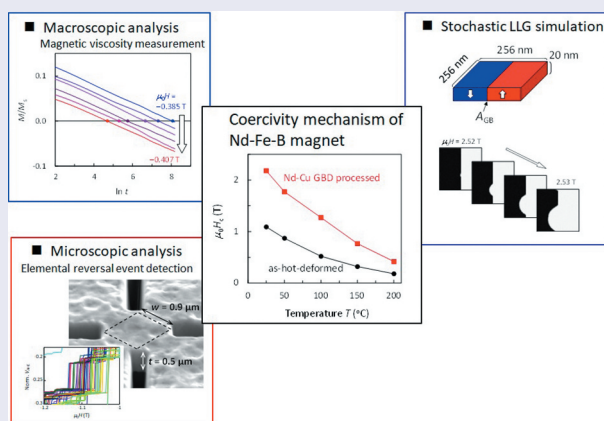
Satoshi Okamoto[a,b,c]

[a]Institute of Multidisciplinary Research for Advanced Materials (IMRAM), Tohoku University, Sendai, Japan;
[b]Center for Spintronics Research Network (CSRN), Tohoku University, Sendai, Japan;
[c]Elements Strategy Initiative Center for Magnetic Materials (ESICMM), National Institute for Materials Science (NIMS), Tsukuba, Japan

ABSTRACT

Although coercivity is one of the fundamental properties of permanent magnets, it has not been well understood. In this paper, micromagnetics and thermal activation magnetization reversal theories are briefly reviewed, and then our recent macroscopic and microscopic experimental approaches for thermally activated magnetization reversal in advanced Nd-Fe-B hot-deformed magnets are explained. Our experimental results are well supported by the recent atomistic spin model calculations. Moreover, the systematic micromagnetics simulation study makes much clearer the physical picture of the thermally activated magnetization reversal process in permanent magnets.

1 Introduction

The development of high-performance Nd-Fe-B magnets without using heavy-rare-earth (HRE) elements has been a critical issue for the traction motor application of electric/hybrid vehicles [1,2]. During the past decade, various kinds of HRE-free Nd-Fe-B magnets have been developed through elaborate microstructure control processes, such as hot-deformation [3], eutectic alloy grain-boundary diffusion [4,5], He-jet-milling press-less processes [6,7], Ga-added and optimal heat-treatment process [8,9], and so on. As an example, Figure 1(a) shows the coercivity H_c of two types of hot-deformed magnets, which are the as-hot-deformed (HD) and Nd-Cu eutectic alloy grain-boundary diffused (GBD) ones, as a function of temperature [10]. Figure 1(b) shows their H_c/H_k as a function of temperature, where H_k is the anisotropy field, which has been regarded as the

ideal upper limit of coercivity. Although the GBD magnet exhibits an approximately two-times larger H_c than that of HD magnet, it remains at one third of H_k. These small values of H_c/H_k have been commonly observed in various permanent magnets, as pointed out by Kronmüller [11]. Moreover, the H_c values of both magnets significantly decrease with increasing temperature. The values of H_c/H_k also decrease with increasing temperature. These facts indicate that the reduction of H_c with temperature cannot be explained only by the reduction of the magnetic anisotropy constant. Therefore, the magnetization reversal process and its change with temperature are essentially important.

The study on the magnetization reversal process of permanent magnets has a long history. About three-quarters of a century ago, Brown pointed out the theoretical difficulties on this issue [12]. Thus, the
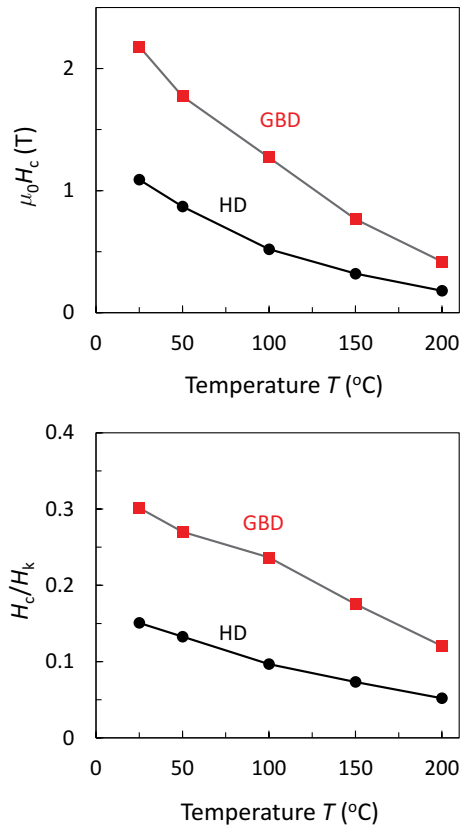
Figure 1. Temperature dependent (a) $\mu_0 H_c$ and (b) H_c/H_k of HD and GBD magnets [10]. These two magnets have the same size of $3 \times 0.5 \times 0.5$ mm^3 with c-axis parallel to the long axis.

lower value of H_c compared with H_k is now referred to as the Brown's paradox. When we discuss the coercivity, we usually measure the field at which the magnetization becomes zero on the magnetization curve at ambient conditions. However, the measured coercivity is the consequence of many elemental processes including nucleation and domain wall depinning/propagation. Both nucleation and domain wall depinning are the breaking events of the equilibrium states. These equilibrium breaking events are initiated by the formation of a small reversed embryo with a size of the order of the exchange length. In this size range, the thermal activation process plays a significant role even in the bulk magnet. In fact, these pictures of magnetization reversal in permanent magnets have been intensively studied by Givord et al. [13–18]. However, there are some ambiguous theoretical points. The most important issue that has not been discussed before is the relationship between the experimentally analyzed H_c, which is macroscopically measured, and the actual microscopic reversal events.

Very recently, theoretical approaches for the microscopic reversal events have advanced significantly. The energy barrier for the thermally activated nucleation was computationally evaluated from the energy landscape calculation with the energy minimizing path method [19,20]. More accurately, the thermally activated nucleation process and its energy

barrier were successfully calculated using the atomistic spin model [21–23]. From the experimental approaches on this issue, we re-examined the micromagnetic coercivity analysis [10,24]. Moreover, the detection of elemental magnetization reversal events and their thermal fluctuation behaviors were successfully performed [25,26].

In this paper, the recent developments of experimental approaches for the magnetization reversal process are reviewed. The micromagnetics and thermal activation theories on the magnetization reversal processes for permanent magnets are briefly reviewed in Section 2. In Section 3, the experimental approaches for the thermally activated magnetization reversal processes are explained from the macroscopic and microscopic measurements. Moreover, stochastic simulation results are explained. Section 4 is the summary.

2. Micromagnetics and thermal activation theories for permanent magnets

2.1 Micromagnetics

Micromagnetics is the mathematical energy-minimization method used to find the equilibrium magnetization state of a finite magnet body, which was originally developed by Brown [27]. Based on this approach, Aharoni formulated the curling- and buckling-type nucleation processes for spheroids and infinite cylinders with a size larger than a certain critical diameter d_c [28–30]. For a sphere, d_c is given as [31],

$$d_c = 2l_{ex} q / \sqrt{N_x} , \qquad (1)$$

where $l_{ex} = \sqrt{2A/\mu_0 M_s^2}$ is the exchange length, q is the geometrical factor approximately given as 2, N_x is the demagnetization factor of the orthogonal direction, A the exchange stiffness, M_s the saturation magnetization, μ_0 the permeability in vacuum. When the grain size is larger than d_c, the magnetization reversal process changes from coherent rotation to nucleation. The value of d_c for Nd$_2$Fe$_{14}$B is evaluated to be as 18 nm. It is widely accepted that the reduction of the grain size in Nd-Fe-B sintered magnets effectively enhances H_c [1,2]. Someone may explain that the enhancement of H_c with decreasing the grain size is attributed to the change in the magnetization reversal process from incoherent to coherent modes. However, the experimentally discussed grain size is about μm range, which is two orders of magnitude larger than the value of d_c. Therefore, it is plausible that the experimentally observed H_c enhancement with decreasing the grain size results from another mechanism rather than the change in the magnetization reversal process. The nucleation field for the grain diameter $d > d_c$ is given in the curling model as [31],

$$H_{\mathrm{n}} = H_k - N_{\mathrm{z}}M_{\mathrm{s}} + \frac{4l_{\mathrm{ex}}^2}{d^2}q^2 M_{\mathrm{s}}, \qquad (2)$$

where N_{z} is the demagnetization factor along the external field. Here, $H_{\mathrm{n}} = H_k - N_{\mathrm{z}}M_{\mathrm{s}}$ is the lowest nucleation field in the curling model for an extremely large d. Thus, the nucleation field decreases from H_{k}, whereas the reduction is not sufficient to fill the gap between the experimentally observed H_{c} and H_{k}. The curling model assumes that the magnetic material is uniform. However, nonuniform magnetic materials including defects and/or grain boundaries have been treated as a one-dimensional model, which is a planar soft magnetic layer sandwiched between two hard magnetic layers [32–36]. By using this model, domain wall depinning and defect-driven nucleation could be theoretically calculated. Through this approach, Kronmüller et al. formulated the following simple equation as [11,37,38],

$$H_c = \alpha H_k - N_{eff}M_s, \qquad (3)$$

where α is the reduction coefficient related to the soft-region magnetic anisotropy and/or easy axis orientation, and N_{eff} is the effective local demagnetization coefficient. Kronmüller et al. studied the physical mechanism for the various cases and found that α was proportional to r_0/δ_{B}, where r_0 is the thickness of the soft magnetic phase and δ_{B} is the domain wall thickness of the hard magnetic phase. Eq. (3) has been widely accepted by experimental researchers to analyze the temperature-dependent H_{c}. By plotting H_c/M_{s} versus H_k/M_{s}, α and N_{eff} are determined by the slope and the y-axis intercept, respectively. This determination assumes that α is invariant against temperature. However, $\alpha \propto r_0/\delta_{\mathrm{B}}$, originally given by Kronmüller, obviously exhibits the temperature dependence. Moreover, many experimental researchers blindly accept the nucleation process when adopting Eq. (3) to the experimental H_{c}. However, from the experimental results of angular-dependent H_{c}, a $1/\cos\theta_{\mathrm{H}}$ type behavior has been observed in various magnets, including Nd-Fe-B sintered, $SmCo_5$ sintered, and ferrite magnets [14], where θ_{H} is the external field direction. Figure 2 shows an example result for GBD magnet [10]. The $1/\cos\theta_{\mathrm{H}}$ type H_{c} behavior is explained well as the dominant magnetization reversal process of domain wall depinning. However, we believe that the actual magnetization reversal is the multiple and simultaneous events of nucleation and domain wall depinning. Therefore, this kind of alternative choice of nucleation and domain wall depinning is too simple to describe the actual magnetization reversal process in permanent magnets.

2.2 Thermal activation model

The micromagnetics theory explained above does not consider the thermal activation process. However, the thermal activation process plays an important role in the magnetization reversal process even in bulk
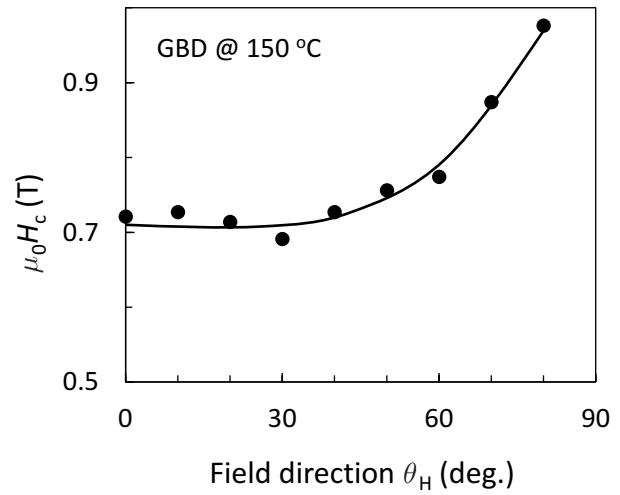
Figure 2. Angular dependent m_0H_c of GBD magnet measured at 150°C [10]. Solid line is a guide to the eye.

magnets. This was classically evidenced by the magnetic viscosity experiments [39]. The magnetic viscosity is the phenomenon in which the magnetization M gradually changes with time t under a constant magnetic field and is empirically described as,

$$M(t) = M(0) - S \ln t \qquad (4)$$

where S is the magnetic viscosity coefficient. S is represented by using the fluctuation field H_{f} and the irreversible magnetic susceptibility χ_{irr} as [40],

$$S = \chi_{irr}H_f \qquad (5)$$

The magnetic viscosity is an ensemble of stochastically occurring elemental magnetization reversal events. The probability $P(H)$ of each event is expressed by the Néel-Arrhenius relaxation law as,

$$P(H) = 1 - exp(-t/\tau(H)) \qquad (6)$$

where τ is the relaxation time given as,

$$1/\tau(H) = f_0 exp(-E_b(H)/k_BT) \qquad (7)$$

where f_0 is the attempt frequency, k_{B} is the Boltzmann constant, and T is the temperature. $E_{\mathrm{b}}(H)$ is the energy barrier generally given as,

$$E_b(H) = E_0(1 - H/H_0)^n \qquad (8)$$

where E_0 and H_0 are the barrier height at $H = 0$ and the intrinsic magnetization reversal field, respectively. $n = 1 \sim 2$ is the constant depending on the magnetization reversal process. The actual magnetic material has a certain amount of E_{b} dispersion. When the E_{b} dispersion is wider than the thermal energy $k_{\mathrm{B}}T$, H_{f} is given as [13],

$$H_f = -\frac{k_BT}{\partial E_b/\partial H}. \qquad (9)$$

Givord pointed out the experimental fact that S and χ_{irr} exhibit identical behaviors against H for various

permanent magnets [14–16,39], and H_f can be treated as a constant from Eq. (5). Thus, E_b is expressed as a linear function against H from Eq. (9), resulting in $n = 1$ in Eq. (8). For the normal magnetization curve measurements which have a data acquisition time of several seconds, E_b corresponds to be $25k_BT$ from Eq. (7). Moreover, assuming the effective reversal field $H = H_c + N_{eff}M_s$, Givord derived the following form of H_c from Eq. (8) with $n = 1$ [14],

$$H_c = \frac{E_0}{M_s v_{act}} - N_{eff}M_s - 25H_f, \qquad (10)$$

where $v_{act} = k_BT/M_sH_f$ is called as activation volume [40]. Assuming $E_0 \propto \gamma_w\delta_w^2$ and $v_{act} \propto \delta_w^3$, the first term on the right-hand side of Eq. (10) becomes in proportion to H_k, where γ_w is the domain wall energy $\propto \sqrt{AK_u}$ and δ_w is the domain wall width $\propto \sqrt{A/K_u}$. Thus, Eq. (10) is similar to Eq. (3), originally proposed by Kronmüller. Note that Eq. (10) is derived by assuming $n = 1$ in the energy barrier function of Eq. (8). Very recently, we proposed the more general analysis of thermally activated magnetization reversal based on magnetic viscosity measurements, as explained in the next section.

## 3. Experimental magnetization reversal analyses for permanent magnets

3.1 Magnetic viscosity analyses

As mentioned above, Givord discussed the thermally activated magnetization reversal by assuming the value of $n = 1$ in the energy barrier function of Eq. (8). However, El-Hilo et al. pointed out that the calculated H_f for the assembly of Stoner-Wohlfarth particles, which has $n = 2$ of Eq. (8), becomes almost constant against H when the E_b distribution is large [41]. This result indicates that we would have the wrong conclusion of $n = 1$ even though the actual value of $n = 2$. Since the value of n significantly affects the evaluated values of E_0 and H_0, the experimental determination of n is very important.

El-Hilo's study also indicates that the calculated H_f at $H \approx H_c$ is insensitive to the E_b distribution. This result means that the evaluation of H_f at $H \approx H_c$ is reliable even if the E_b distribution exists. Conventionally, H_f has been evaluated from the separately measured S and χ_{irr} based on Eq. (5). In contrast, El-Hilo also proposed the H_f evaluation only from the magnetic viscosity measurements as,

$$H_f = -\frac{\Delta H}{\Delta \ln(S/t)}. \qquad (11)$$

This evaluation of H_f is expected to have a higher accuracy than the conventional method because the measurement of χ_{irr} is unnecessary. As an example, the magnetic viscosity curves of the GBD magnet for various H around H_c are shown in Figure 3(a). From
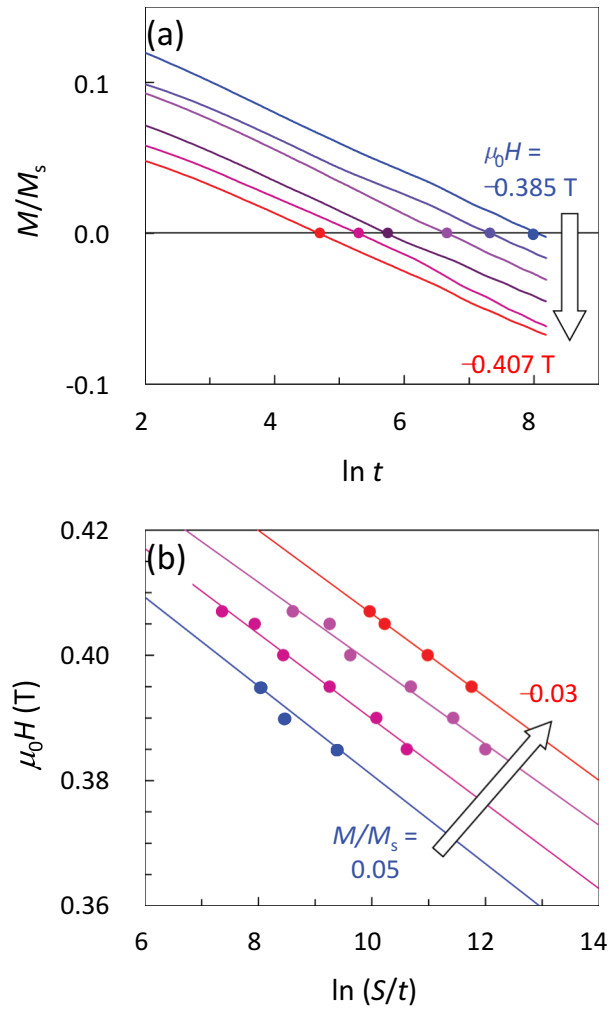

Figure 3. (a) Magnetic viscosity curves of GBD magnet measured at 200°C under various values of m_0H near m_0Hc [10]. Solid marks in (a) correspond to time dependent m_0Hc. (b) H versus ln(S/t) for each constant M/Ms evaluated from (a).

these viscosity data, H versus $\ln(S/t)$ are plotted in Figure 3(b). From this plot, H_f is evaluated using Eq. (11). We have experimentally confirmed that the value of H_f from Eq. (11) is identical to that from Eq. (5) [24].

The intersection points of the viscosity curves with the transverse line of $M/M_s = 0$ in Figure 3(a) correspond to the time dependent H_c, as plotted in Figure 4 (a). This is formulated from $P(H) = 0.5$ of Eq. (6) as,

$$H_c(t) = H_0\left[1 - \left\{\frac{k_BT}{E_0}\ln\left(\frac{f_0t}{\ln(2)}\right)\right\}^{1/n}\right]. \qquad (12)$$

This equation was first proposed by Sharrock [42,43]. The value of $f_0 = 1 \times 10^{11}$ Hz is used in this study [10,44,45]. The solid line in Figure 4(a) is the best fitting result. The determination of n is difficult from this fitting because the fitting of Eq. (12) is possible for a certain range of n. Therefore, the values of E_0 and H_0 are evaluated by varying n, and then the H_f curve against n from Eq. (9) is obtained, as shown by the red line in Figure 4(b). The value of H_f should agree with that from the magnetic viscosity curve analysis, as
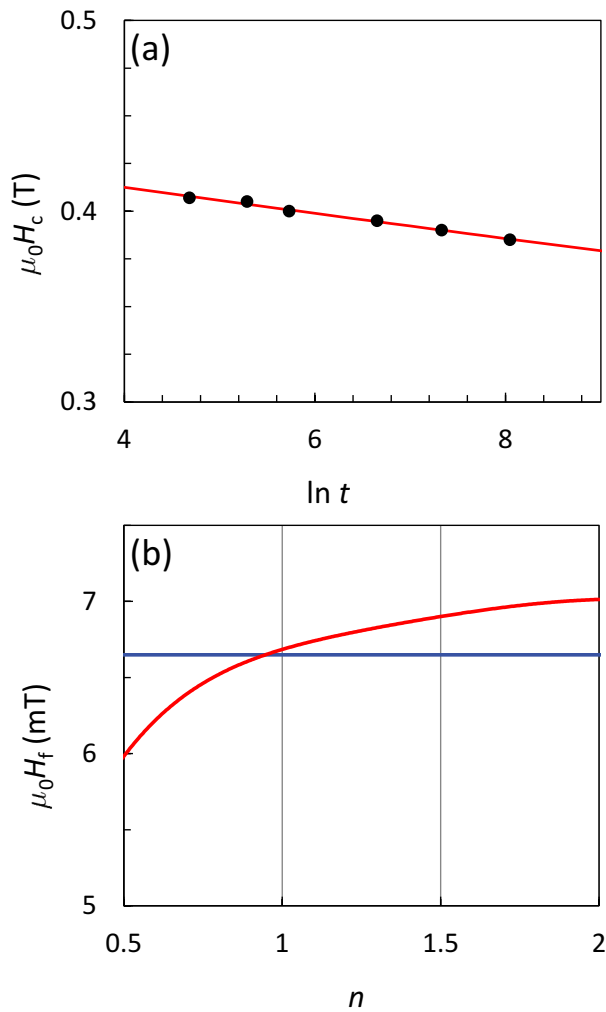
Figure 4. (a) Time dependent m_0H_c obtained from Fig. 3(a). Solid line is the best fitting of Eq. (12). (b) m_0H_f (red curve) evaluated from the time dependent m_0H_c in (a) as a function of n of Eq. (12). Blue line is the value of m_0H_f evaluated from the viscosity experiment (Fig. 3(b)).

shown by the blue line in Figure 4(b), consequently all the parameters of E_0, H_0, and n are fixed.

Figure 5 shows the values of E_0, H_0, and n for HD and GBD magnets at various temperatures. As shown in Figure 1(a), these two magnets exhibit quite different H_c, and their temperature dependences are quite large. The values of H_0 exhibit the similar trends of H_c for these two magnets, whereas the values of n are almost 1 and insensitive to the samples and temperature. Eventually, the assumption of $n = 1$ by Givord [14] is verified. Previously, the value of n reflects the magnetization reversal process, i.e., $n = 2$ for coherent rotation and $n = 1$ for weak domain wall pinning [13,46]. Recently, however, $n = 1$ is supported theoretically when the two following conditions are fulfilled. One is a sufficiently large magnet body compared with the exchange length, and the second is a sufficiently slow magnetization reversal compared with the relaxation of magnetization [47]. Very recently, Toga rigorously verified this picture using the energy landscape calculation based on the atomistic spin model [23]. Obviously,

these two conditions are quite reasonable for magnetization reversal in permanent magnets irrespective of the magnetization reversal processes, i.e., nucleation or domain wall depinning.

Interestingly, the values of E_0 are on the order of 10^{-19} J and are almost insensitive to temperature. This value of E_0 is on the same order as $\gamma_w\delta_w{}^2$, clearly indicating that the nucleation or domain wall depinning initiated from the formation of the reversed embryo with the domain wall width. More details on E_0 are discussed in the next section.

3.2 Detection of elemental magnetization reversal events

Thermally activated magnetization reversal is discussed in the preceding section. As mentioned in Section 1, however, the macroscopically measured H_c is the consequence of numerous elemental magnetization reversal events. Therefore, it is essential to detect the elemental magnetization reversal events directly. Very recently, we have directly detected elemental magnetization reversal events in Nd-Fe-B hot-deformed magnets [25,26]. With careful evaluation of the process damage on the magnetic properties, a submicron cross-shaped pattern of Nd-Fe-B hot-deformed magnet was fabricated using mechanical polishing and focused-ion beam (FIB), as shown in Figure 6(a). The c-axis of $Nd_2Fe_{14}B$ is along the plane normal. The magnetic signal from this extremely small cross-center area was sensitively detected using anomalous Hall effect (AHE) measurement with a sweeping H. When the cross-center area is on the order of 10 μm square, the AHE curve is the same as that of the unpatterned sample. The AHE curve for the sample shown in Figure 6(a), however, becomes a staircase in which each step corresponds to the elemental magnetization reversal event. Figure 6(b) shows an example of one step of the AHE curve repeatedly measured 50 times. The step height corresponds to one or two grain magnetization reversal. Note that the reversal field of this step fluctuates about 0.1 T. Figure 6(c) shows the reversal probability P (H) as a function of H. This can be fitted well with the following function derived from the integration of the Néel-Arrhenius relaxation law of Eq. (6) for a constant field sweep rate R,

$$P(H) = 1 - \exp\left\{-\frac{f_0\exp[-(E_0/k_BT)(1-H/H_0)^n]}{n(R/H_0)(E_0/k_BT)(1-H/H_0)^{n-1}}\right\}.$$

(13)

As mentioned above, the value of $n = 1$ is adopted for the fitting in Figure 6(c), and $f_0 = 1 \times 10^{11}$ Hz is used. This very good reproducibility of $P(H)$ curve clearly evidences that the experimentally observed step fluctuation is caused by thermal fluctuation. Thus, the values of E_0 and H_0 are evaluated for each step of the AHE curve.
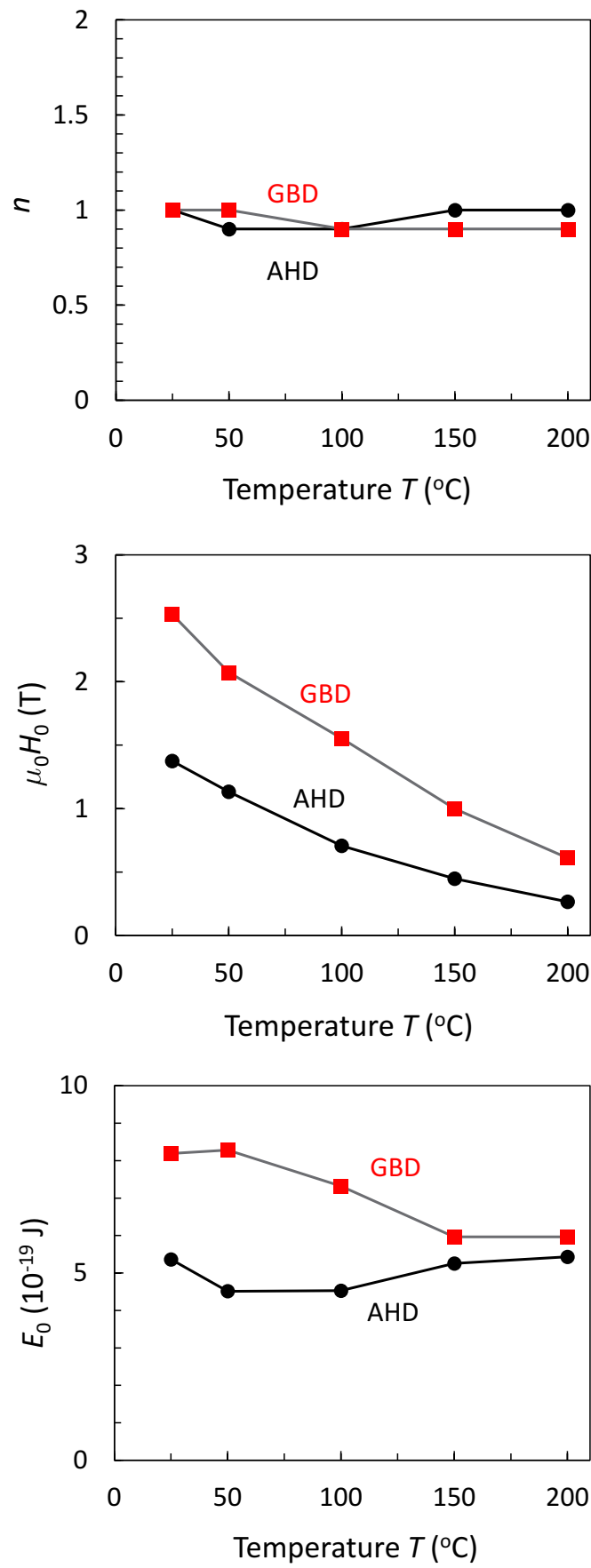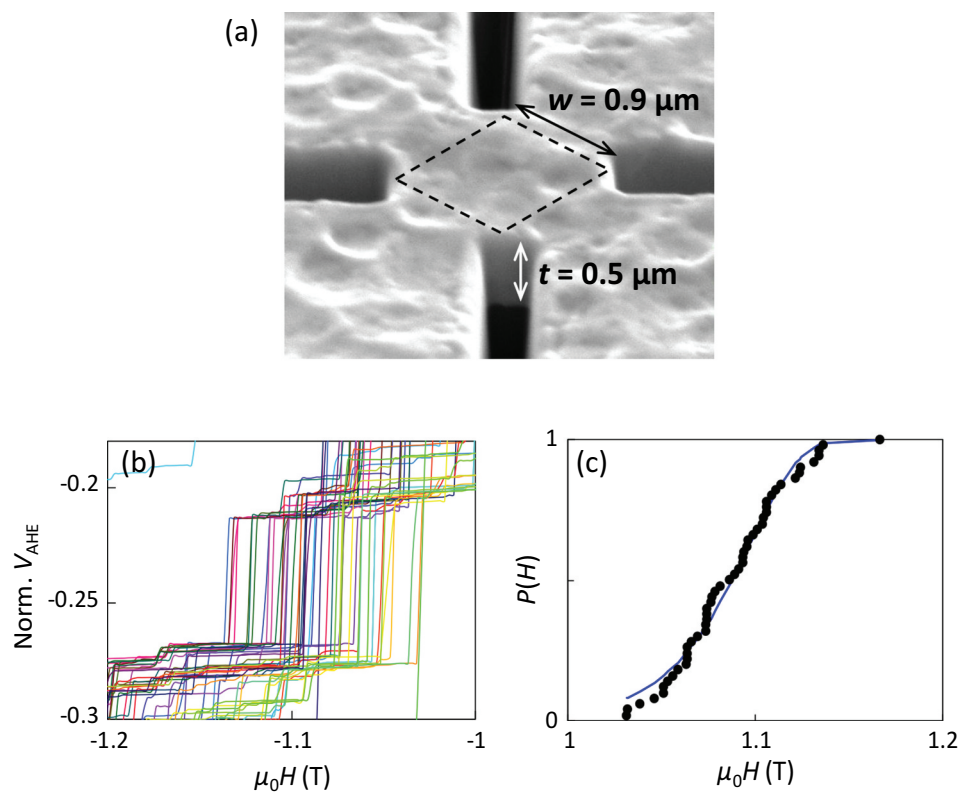
Figure 5. Temperature dependent (a) n, (b) $m_0 H_0$, and (c) E_0 of HD and GBD magnets [10].

Figure 6. (a) AHE cross-shaped Nd-Fe-B hot-deformed magnet fabricated by FIB. (b) One step pattern of repeatedly measured 50 AHE curves. (c) Probability curve $P(H)$ of the thermally fluctuated magnetization reversal of the step in (a). Blue curve in (b) is the best fitting of eq. (13) [26].

This analysis is adopted for the three Nd-Fe-B hot-deformed magnets (Samples A ~ C) with different $\mu_0 H_c$ values of 2.0, 1.8, and 2.2 T. Sample A of $Nd_{23.4}Pr_{7.5}$ $Fe_{bal.}Co_{3.5}B_{0.9}Ga_{0.5}$ (wt. %) is regarded as the standard among them. Sample B of $Nd_{22.1}Pr_{7.0}Fe_{bal.}Co_{3.5}B_{0.9}$ $Ga_{0.5}$ (wt. %) has a somewhat lower Nd composition than Sample A. Sample C is the Nd-Cu eutectic alloy grain-boundary diffusion processed magnet of Sample A. For each magnet, eight or nine steps are analyzed, and the relationships between E_0 and H_0 are plotted in Figure 7. Although there are large dispersions of the data points, some trends can be found. First, very wide dispersion of H_0 is found. Second, the slope of E_0 against H_0 for Samples A and C is small whereas it becomes large for Sample B, as depicted by the broken lines in Figure 7.

To understand these behaviors, computer simulation based on the Landau-Lifshitz-Gilbert (LLG) equation was performed using MuMax3 software [48]. A two-grain model was employed, as schematically shown in Figure 8(a). The model size is 256 nm in width and 20 nm in height with 1 nm cubic meshes. The center (xz) plane corresponds to the grain boundary, and the right and left grains are initially set to be the up and down magnetization states, respectively. To eliminate the effect of the very strong demagnetization field from the outer boundary, periodic boundary conditions are given for the x-, y-, and z-axes. The magnetic easy axis is along the z-axis. A random field corresponding to
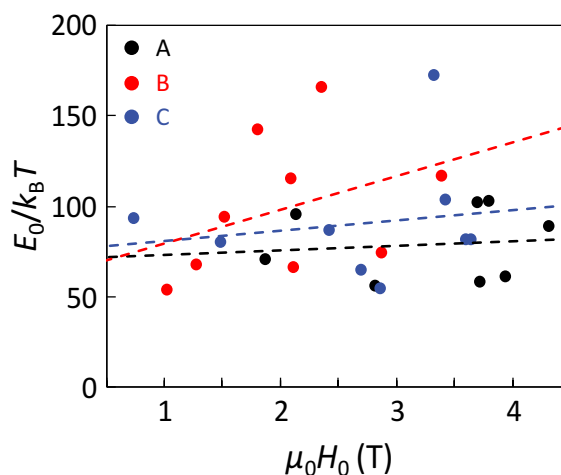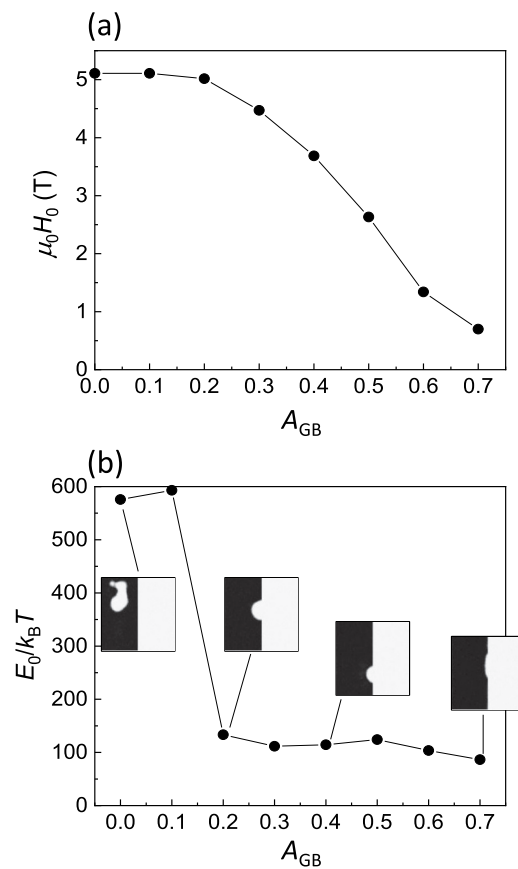

Figure 7. Relationship between $E_0/k_B T$ and H_0 for Samples A, B, and C. Broken lines are the linear fittings as eye guides [26].

a thermal energy of 300 K is given to simulate the thermally activated magnetization reversal. The magnetic anisotropy and exchange stiffness are identical to those of $Nd_2Fe_{14}B$ [49,50]. The domain wall depinning process strongly depends on the many parameters of grain boundary phase such as magnetization, magnetic anisotropy, exchange stiffness, and thickness. In this study, for simplicity, the parameter A_{GB} is introduced as the dimensionless exchange stiffness at the grain boundary with respect to that of $Nd_2Fe_{14}B$, which
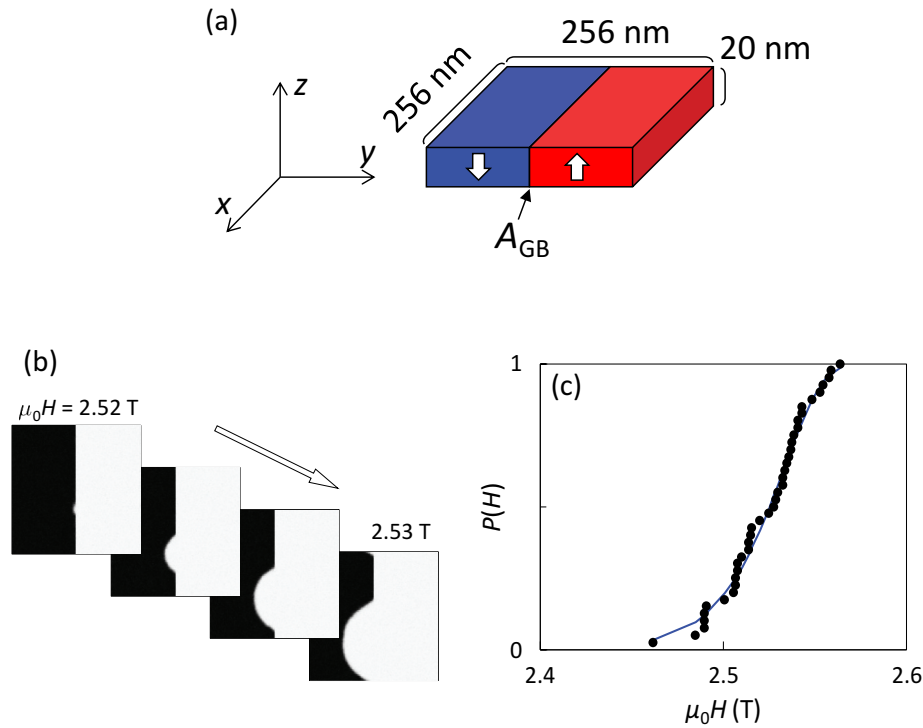
Figure 8. (a) Schematic illustration of the two-grain model using in the LLG simulation. A_{GB} is normalized intergrain exchange stiffness with respect to the exchange stiffness of $Nd_2Fe_{14}B$ (b) Calculated snapshot images of the z-component of magnetization for the domain-wall depinning process with continuously varying field H. (c) Probability curve $P(H)$ of the thermally fluctuated domain-wall depinning. Blue curve in (c) is the best fitting of eq. (13) [26].

involves the effects of all these grain boundary parameters. Figure 8(b) shows snapshot images of the magnetization reversal, indicating that the thermally activated domain wall depinning is initiated by the formation of a very small reversed embryo with the size of nanometer range. As well as the experiment shown in Figure 6(c), the reversal probability $P(H)$, an example shown in Figure 8(c), is obtained as a function of H by 40 times repeated calculations. Thus, the values of E_0 and H_0 are obtained from the simulation. Figure 9 shows the thus evaluated E_0 and H_0 as a function of A_{GB} varying from 0 to 0.7. For $A_{GB} > 0.7$, the domain wall cannot be pinned at the grain boundary. H_0 gradually increases with decreasing A_{GB} and is saturated for $A_{GB} \leq 0.2$. On the other hand, E_0 keeps almost constant for $A_{GB} \geq 0.2$ and then rapidly increases for $A_{GB} \leq 0.1$. The snapshot images at which the magnetization reversal just begins are shown as the insets of Figure 9(b). For $A_{GB} \geq 0.2$, the thermally activated domain wall depinning is clearly confirmed. In contrast, for $A_{GB} \leq 0.1$, the nucleation inside the domain occurs instead of domain wall depinning, indicating that the magnetization reversal process discretely changes from domain wall depinning to nucleation. Figure 10 shows the relationship between E_0 and H_0 evaluated from the simulation. In this figure, the data for $A_{GB} \leq 0.1$ are excluded because of the different magnetization reversal process from that for $A_{GB} > 0.2$. To discuss the effect of the magnetic properties of the main phase, the magnetic anisotropy

Figure 9. (a) m_0H_0 and (b) E_0/k_BT evaluated from the fitting of eq. (13) as a function of A_{GB}. Insets in (b) are the snapshot images at which domain wall depinning just began.
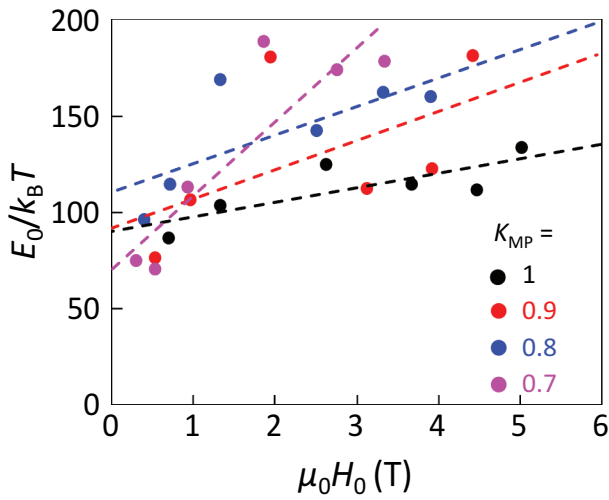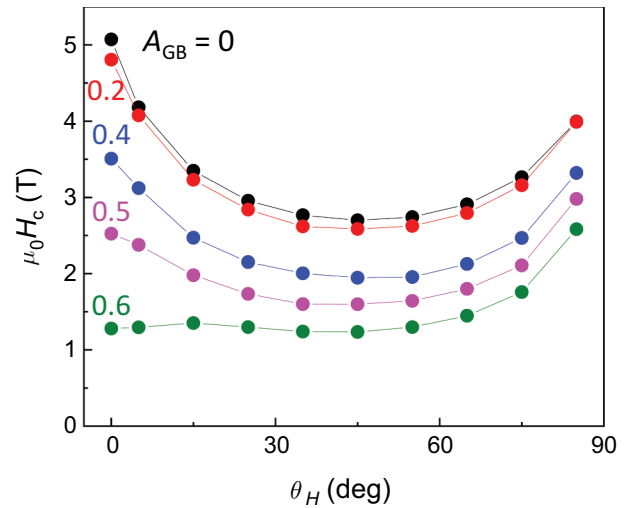
Figure 10. Relationship between E_0/k_BT and m_0H_0 obtained from the LLG simulation for various values of K_{MP}. Broken lines are the linear fitting as eye guides [26].

Figure 11. Angular dependent µ0Hc obtained from the LLG simulation for various values of A_{GB}.

K_{MP} with respect to that of $Nd_2Fe_{14}B$ is varied. For K_{MP} = 1 (i.e., no deterioration of magnetic anisotropy), E_0 exhibits little dependence on H_0. This behavior is consistent with the experimental results of Samples A and C in Figure 7. On the other hand, the slope of E_0 against H_0 becomes steeper with decreasing K_{MP}. This seems consistent with that of Sample B, which exhibits the lowest H_c among the three samples studied in this work.

These results lead to some insights into thermally activated domain wall depinning. First, A_{GB} only affects the critical field of domain wall depinning. Second, E_0 is determined by the main phase magnetic properties because E_0 is the critical energy for the expansion of the domain wall depinning nucleus, which is grown inside the main phase grain. In particular, because the domain wall depinning nucleus is on the order of the domain wall thickness, E_0 strongly reflects the magnetic properties of the surface of the main phase grain.

Finally, the angular dependence of H_c is calculated using the two grain model. Figure 11 shows H_c as a function of the field direction θ_H with respect to the magnetic easy axis for various A_{GB} including the range of nucleation and domain wall depinning as discussed above. For A_{GB} = 0, at which the nucleation occurs inside the main phase grain, the asteroid curve-like behavior is clearly obtained. H_c at θ_H = 0 ° gradually decreases with increasing A_{GB}, and then the angular dependence of H_c becomes close to the behavior of $1/cos\theta_H$. As mentioned above, the magnetization reversal process changes from nucleation to domain wall depinning at A_{GB} = 0.2 discontinuously, and E_0 suddenly changes at A_{GB} = 0.2, as shown in Figure 9(b). However, the angular dependence of H_c for A_{GB} = 0.2 still exhibits asteroid curve-like behavior. The angular dependences of H_c for A_{GB} = 0.4 and 0.5 are close to the asteroid curve-like behavior rather than the $1/cos\theta_H$-

like behavior. These results suggest that the identification of the magnetization reversal process of the nucleation or domain wall depinning process is quite difficult only from the angular dependence of H_c.

4 Summary

In this paper, we reviewed the coercivity mechanism and its analyses for permanent magnets. Previously, it has been widely believed that the thermal activation process is not important in the magnetization reversal of permanent magnets because permanent magnets are bulk materials. As discussed in this paper, however, the thermal activation process, which forms a small reversed embryo with a size on the order of nanometers, plays a critical role in the magnetization reversal of permanent magnets.

We studied the macroscopic and microscopic approaches for the thermally activated magnetization reversal process in advanced Nd-Fe-B hot-deformed magnets. Through these studies, the physical picture of the thermal activation process becomes much clearer. Moreover, we would like to emphasize that the energy barrier parameters discussed in this paper strongly reflect the magnetic properties of the grain boundary phase and grain surface. In fact, the modern advanced magnets have been developed for the purpose of improving the magnetic properties of the grain boundary phase and grain surface. However, their direct evaluation is not easy. The energy barrier analysis is expected to be an evaluation method for them.

Disclosure statement

No potential conflict of interest was reported by the author.

Funding

Notes on contributor

Satoshi Okamoto was born in Shiga, Japan in 1968. He received his PhD in 1997 from Tohoku University. He was then appointed as an Assistant Professor at Research Institute for Scientific Measurements (RISM) in Tohoku University in 1997 and promoted to as an Associate Professor at Institute of Multidisciplinary Research for Advanced Materials (IMRAM) in Tohoku University in 2007. Since 2020, he has been a Professor of IMRAM in Tohoku University. He has also worked as a Principle Investigator of Elements Strategy Initiative Center for Magnetic Materials (ESICMM) since 2014 and a Guest Senior Researcher of National Institute for Materials Science (NIMS) since 2019. His current interest is focused on the relationship between nanoscale spindynamics and macroscopic functionalities of magnetic devices.

References

[1] Hono K, Sepehri-Amin H. Strategy for high-coercivity Nd–Fe–B magnets. Scr Mater. 2012;67:530–535.

[2] Hirosawa S. Current status of research and development toward permanent magnets free from critical elements. J Magn Soc Jpn. 2015;39:85–95.

[3] Hioki K, Hattori A, Iriyama T. Development of Dy-Free hot-deformed Nd-Fe-B magnets by optimizing chemical composition and microstructure. J Magn Soc Jpn. 2014;38:79–82.

[4] Sepehri-Amin H, Ohkubo T, Nishiuchi T, et al. Coercivity enhancement of hydrogenation–disproportionation-desorption-recombination processed Nd-Fe-B powders by the diffusion of Nd–Cu eutectic alloys. Scr Mater. 2010;63:1124–1127.

[5] Akiya T, Liu J, Sepehri-Amin H, et al. Low temperature diffusion process using rare earth-Cu eutectic alloys for hot-deformed Nd-Fe-B bulk magnets. Scr Mater. 2014;81:48–51.

[6] Une Y, Sagawa M. Enhancement of coercivity of Nd-Fe-B sintered magnets by grain size reduction. J Jpn Inst Metals. 2012;76:12–16.

[7] Nakamura M, Matsuura M, Tezuka N, et al. Preparation of ultrafine jet-milled powders for Nd-Fe-B sintered magnets using hydrogenation–disproportionation–desorption–recombination and hydrogen decrepitation processes. Appl Phys Lett. 2013;103:022404.

[8] Nakamura K, Yamazaki T. Japan Patent 2015: 5767788.

[9] Sasaki T, Ohkubo T, Takada Y, et al. Formation of non-ferromagnetic grain boundary phase in a Ga-doped Nd-rich Nd-Fe-B sintered magnet. Scr Mater. 2016;113:218–221.

[10] Okamoto S, Goto R, Kikuchi N, et al. Temperature-dependent magnetization reversal process and coercivity mechanism in Nd-Fe-B hot-deformed magnets. J Appl Phys. 2015;118:223903.

[11] Kronmüller H. Theory of nucleation fields in inhomogeneous ferromagnets. Phys Stat Sol (B). 1987;144:385–396.

[12] Brown WF. Virtues and weaknesses of the domain concept. Rev Mod Phys. 1945;17:15–19.

[13] Gaunt P. Magnetic viscosity and thermal activation energy. J Appl Phys. 1986;59:4129–4132.

[14] Givord D, Tenaud P, Viadieu T. Coercivity mechanisms in ferrites and rare earth transition metal sintered magnets ($SmCo_5$, Nd-Fe-B). IEEE Trans Magn. 1988;24:1921–1923.

[15] Givord D, Tenaud P, Viadieu T, et al. Magnetic viscosity in different NdFeB magnets. J Appl Phys. 1987;61:3454–3456.

[16] Givord D, Lienard A, Tenaud P, et al. Magnetic viscosity in Nd-Fe-B sintered magnets. J Magn Magn Mater. 1987;67:L281–L285.

[17] Givord D, Lu Q, M F R, et al. Experimental approach to coercivity analysis in hard magnetic materials. J Magn Magn Mater. 1990;83:183–188.

[18] Givord D, Rossignol M, Barthem VMTS. The physics of coercivity. J Magn Magn Mater. 2003;1–5:258–259.

[19] Bance S, Fischbacher J, Schrefl T. Thermally activated coercivity in core-shell permanent magnets. J Appl Phys. 2015;117:17A733.

[20] Bance S, Fischbacher J, Kovacs A, et al. Thermal activation in permanent magnets. JOM. 2015;67:1350–1356.

[21] Miyashita S, Nishino M, Toga Y, et al. Perspectives of stochastic micromagnetism of $Nd_2Fe_{14}B$ and computation of thermally activated reversal process. Scr Mater. 2018;154:259–265.

[22] Toga Y, Matsumoto M, Miyashita S, et al. Monte Carlo analysis for finite-temperature magnetism of $Nd_2Fe_{14}B$ permanent magnet. Phys Rev B. 2016;94:174433.

[23] Toga Y, Miyashita S, Sakuma A, et al. Role of atomic-scale thermal fluctuations in the coercivity. NPJ Comput Mater. 2020;6:67.

[24] Goto R, Okamoto S, Kikuchi N, et al. Energy barrier analysis of Nd-Fe-B thin films. J Appl Phys. 2015;117:17B514.

[25] Yomogita T, Kikuchi N, Okamoto S, et al. Detection of elemental magnetization reversal events in a micro-patterned Nd-Fe-B hot-deformed magnet. AIP Adv. 2019;9:125052.

[26] Yomogita T, Okamoto S, Kikuchi N, et al. Direct detection and stochastic analysis on thermally activateddomain-wall depinning events in micropatterned Nd-Fe-Bhot-deformed magnets. Acta Mater. 2020;201:7–13.

[27] Brown WF. Micromagnetics. New York ; London : J. Wiley; 1963.

[28] Aharoni A. Magnetization curling. Phys Stat Sol (B). 1966;16:3–42.

[29] Aharoni A. Curling nucleation eigenvalue in a prolate spheroid. IEEE Trans Magn. 1998;34:2175–2176.

[30] Aharoni A. Magnetization buckling in a prolate spheroid. J Appl Phys. 1986;60:1118–1123.

[31] Bertotti G. Hysteresis in magnetism. Elsevier, USA: Academic Press; 1998.

[32] Craik J, Hill E. Magnetic-domain-wall pinning by regions of weak exchange or anisotropy. Phys Lett A. 1974;48:157–158.

[33] Friedberg R, Paul DI. New theory of coercive force of ferromagnetic materials. Phys Rev Lett. 1974;34:1234–1237.

[34] Zijlstra H. Coping with Brown's paradox: the pinning and nucleation of magnetic domain walls at antiphase boundaries. IEEE Trans Magn. 1979;15:1246–1250.

[35] Paul DI. General theory of the coercive force due to domain wall pinning. J Appl Phys. 1982;53:1649–1654.

[36] Sakuma A, Tanigawa S, Tokunaga M. Micromagnetic studies of inhomogeneous nucleation in hard magnets. J Magn Magn Mater. 1999;84:52–58.

[37] Kronmüller H, Durst K-D, Sagawa M. Analysis of the magnetic hardening mechanism in RE-FeB permanent magnets. J Magn Magn Mater. 1988;74:291–302.

[38] X C K, Kronmüller H, Givord D, et al. Coercivity mechanism of sintered $Pr_{17}Fe_{75}B_8$ and $Pr_{17}Fe_{53}B_{30}$ permanent magnets. Phys Rev B. 1994;50:3849–3860.

[39] Street R, Woolley JC. A study of magnetic viscosity. Proc Phys Soc A. 1949;62:562–572.

[40] Wohlfarth EP. The coefficient of magnetic viscosity. J Phys F Met Phys. 1984;14:L155–L159.

[41] El-Hilo M, O'Grady K, Chantrell RW. Fluctuation fields and reversal mechanisms in granular magnetic systems. J Magn Magn Mater. 2002;248:360–373.

[42] Sharrock M, McKinney J. Kinetic effects in coercivity measurements. IEEE Trans Magn. 1981;17:3020–3022.

[43] Sharrock M. Time dependence of switching fields in magnetic recording media. J Appl Phys. 1994;76:6413–6418.

[44] Brown WF. Relaxational behavior of fine magnetic particles. J Appl Phys. 1959;30:S130–S132.

[45] Brown WF. Thermal fluctuations of a single-domain particle. J Appl Phys. 1969;34:1319–1320.

[46] Gaunt P. Ferromagnetic domain wall pinning by a random array of inhomogeneities. Philos Mag B. 1983;48:261–276.

[47] Vries J, Bolhuis T, Abelmann L. Temperature dependence of the energy barrier and switching field of sub-micron magnetic islands with perpendicular anisotropy. N J Phys. 2017;19:093019.

[48] Vansteenkiste A, Leliaert J, Dvornik M, et al. The design and verification of MuMax3. AIP Adv. 2014;4:107133.

[49] Hirosawa S, Matsuura Y, Yamamoto H, et al. Magnetization and magnetic anisotropy of $R_2Fe_{14}B$ measured on single crystals. J Appl Phys. 1986;59:873–879.

[50] Ono K, Inami N, Saito K, et al. Observation of spin-wave dispersion in Nd-Fe-B magnets using neutron brillouin scattering. J Appl Phys. 2014;115:17A714.